Spatiotemporal evolution of dike opening and décollement slip at Kīlauea Volcano, Hawai'i

E. K. Montgomery-Brown,[1,2] D. K. Sinnett,[1] K. M. Larson,[3] M. P. Poland,[4] P. Segall,[1] and A. Miklius[4]

Received 7 July 2010; revised 23 November 2010; accepted 4 January 2011; published 23 March 2011.

[1] Rapid changes in ground tilt and GPS positions on Kīlauea Volcano, Hawai'i, are interpreted as resulting from a shallow, two-segment dike intrusion into the east rift zone that began at 1217 UTC (0217 HST) on 17 June 2007 and lasted almost 3 days. As a result of the intrusion, a very small volume of basalt (about 1500 m^3) erupted on 19 June. Northward tilt at a coastal tiltmeter, subsidence of south flank GPS sites, southeastward displacements at southwestern flank GPS sites, and a swarm of flank earthquakes suggest that a slow slip event occurred on the décollement beneath Kīlauea's south flank concurrent with the rift intrusion. We use 4 min GPS positions that include estimates of time-dependent tropospheric gradients and ground tilt data to study the spatial and temporal relationships between the two inferred shallow, steeply dipping dike segments extending from the surface to about 2 km depth and décollement slip at 8 km depth. We invert for the temporal evolution of distributed dike opening and décollement slip in independent inversions at each time step using a nonnegative least squares algorithm. On the basis of these inversions, the intrusion occurred in two stages that correspond spatially and temporally with concentrated rift zone seismicity. The dike opening began on the western of the two segments before jumping to the eastern segment, where the majority of opening accumulated. Dike opening preceded the start of décollement slip at an 84% confidence level; the latter is indicated by the onset of northward tilt of a coastal tiltmeter. Displacements at southwest flank GPS sites began about 18 h later and are interpreted as resulting from slow slip on the southwestern flank. Additional constraints on the evolution of the intrusion and décollement slip come from inversion of an Envisat interferogram that spans the intrusion until 0822 UTC on 18 June 2007, combined with GPS and tilt data. This inversion shows that up to 0822 UTC on 18 June, décollement slip is only required in a limited region offshore of Ka'ena Point. A similar inversion of the complete event, which includes GPS and tilt data up to 21 June and a second Envisat interferogram spanning the complete intrusion until 21 June, shows décollement slip spread westward across the south flank. This may suggest westward migration of the décollement slip as the event progressed.

Citation: Montgomery-Brown, E. K., D. K. Sinnett, K. M. Larson, M. P. Poland, P. Segall, and A. Miklius (2011), Spatiotemporal evolution of dike opening and décollement slip at Kīlauea Volcano, Hawai'i, *J. Geophys. Res.*, *116*, B03401, doi:10.1029/2010JB007762.

1. Introduction

[2] A dike intrusion in Kīlauea's upper east rift zone (ERZ) starting 17 June 2007 was recorded in unprecedented spatial and temporal detail by Global Positioning System (GPS), ground tilt, and interferometric synthetic aperture radar (InSAR) data. The intrusion also produced a small (~1500 m^3) eruption 5–10 km up rift of the ongoing Pu'u 'Ō'ō-Kupaianaha eruption [*Poland et al.*, 2008]. Deformation and seismicity were monitored by the Hawaiian Volcano Observatory (HVO) and by InSAR satellites. Primary observations include radially inward tilts at summit area tiltmeters, increased upper ERZ seismicity, and rapid southward tilt at a tiltmeter (ESC) in the ERZ between Pauahi Crater and Mauna Ulu [*Poland et al.*, 2008]. These signals were similar to those observed at the onset of previous intrusions and were quickly followed by extension across the ERZ GPS baseline NUPM-KTPM and a large tilt signal at Pu'u 'Ō'ō.

[1]Department of Geophysics, Stanford University, Stanford, California, USA.
[2]Now at Department of Geoscience, Madison, Wisconsin, USA.
[3]Department of Aerospace Engineering Sciences, University of Colorado at Boulder, Boulder, Colorado, USA.
[4]U.S. Geological Survey, Hawaiian Volcano Observatory, Hawai'i National Park, Hawaii, USA.

0148-0227/11/2010JB007762

[3] Seismic and geodetic measurements indicated three additional pulses of intrusion over the next 56 h. Although ground cracking was extensive, only a small volume of lava was erupted just north of Makaopuhi Crater. The end of the intrusion was marked by a decline in rift zone seismicity and a return to extensional deformation across the summit caldera. As in previous upper ERZ intrusions [*Owen et al.*, 2000a; *Cervelli et al.*, 2002a], Pu'u 'Ō'ō temporarily ceased erupting sometime during the intrusion. Previous ERZ intrusions that have been modeled as uniform opening dislocations typically have about 1–2 m of opening [*Owen et al.*, 2000a; *Cervelli et al.*, 2002a] and extend from the near surface to depths of ~2 km. These depths are consistent with the neutral buoyancy interval in which magmas migrate out into the active upper rift zones [*Ryan*, 1987, 1988] and from which the near-surface intrusions potentially draw their magma. An analysis of cumulative deformation resulting from this event [*Montgomery-Brown et al.*, 2010] shows that this dike also opened ~2 m.

[4] *Montgomery-Brown et al.* [2010] tested a variety of intrusion scenarios and found that models with a single opening dislocation were insufficient to explain the near-field deformation but provided rough constraints on the geometric parameters that adequately describe the intrusion. They tested three more complex models including (1) a curving dike that followed the surface trace of the ERZ, (2) a curving dike that followed the symmetry axis of the deformation seen in radar interferograms spanning the intrusion, and (3) a pair of en echelon dikes. The en echelon dikes provided the best fit to the data.

[5] GPS displacements on Kīlauea's southwest flank, northward tilt at KAE, coastal subsidence, and flank seismicity, suggest that décollement slip occurred during the June 2007 intrusion [*Brooks et al.*, 2008; *Montgomery-Brown et al.*, 2010]. Displacements at southwestern flank GPS sites far from the ERZ are not well fit by models that include only a dike; this was not the case in previous intrusions (e.g., January 1997, September 1999). Rather, displacements at these sites are similar to those observed during previous slow slip events [*Cervelli et al.*, 2002b; *Brooks et al.*, 2006; *Montgomery-Brown et al.*, 2009]. In addition, the coastal tiltmeter, KAE, tilted down to the north during the June 2007 intrusion. Tilts predicted at this site based on a slip model of the 2005 slow slip event [*Segall et al.*, 2006] are also northward and consistent with the 2007 observation. In contrast, southward tilts at KAE are predicted by all shallow rift zone dike models constrained to the zone of cracking and seismicity, opposite in direction from the observed tilts. Finally, a swarm of flank earthquakes which has been observed to accompany previous slow slip events [*Brooks et al.*, 2006; *Segall et al.*, 2006; *Wolfe et al.*, 2007], but not recent intrusions, occurred during the 2007 intrusion. Together, these observations suggest that a slow slip event occurred sometime during the intrusion [*Brooks et al.*, 2008; *Montgomery-Brown et al.*, 2010].

[6] *Dieterich* [1988] noted that feedback between rift intrusion and flank spreading along a nearly horizontal décollement under the south flank of Kīlauea allow for the persistence of volcanic rift zones. This suggests that scenarios involving intrusions triggering flank slip, or vice versa, are equally plausible. Establishing the temporal relationship between the intrusion and the slow slip, therefore, is critical to understanding Kīlauea's mechanical behavior, and could be important in forecasting future flank slip events.

[7] The objective of this paper is to understand the spatiotemporal evolution of dike opening and décollement slip during the June 2007 intrusion. We first invert geodetic data for a time-dependent model of dike opening and décollement slip. We then invert for two models of cumulative deformation including Envisat interferograms, which provide denser spatial sampling of the deformation. The first Envisat interferogram shows cumulative deformation until midway through the intrusion, while the second covers the entire event. These images, combined with GPS positions and ground tilt data up to the times of the second acquisition in each interferogram, allow for models with higher spatial resolution at these two times.

2. Data

2.1. Subdaily GPS Processing

[8] Standard methods of studying deformation with GPS data typically involve differencing the positions before and after the event of interest [e.g., *Owen et al.*, 2000a; *Cervelli et al.*, 2002a; *Montgomery-Brown et al.*, 2010]. In the case of events that last from weeks to months, it is possible to follow the progression of the activity through time with daily GPS solutions [e.g., *Bonaccorso et al.*, 2002; *Desmarais and Segall*, 2007; *Lisowski et al.*, 2008]. However, the evolution of magmatic events that take place over much shorter time spans are unresolvable using 24 h averaged positions. Improvements in the GPS constellation, receiver technology, and data processing models in the last decade have led to more precise subdaily positions, which in turn allow us to model the progress of intrusions that occur on shorter timescales.

[9] In this study, GPS data from 19 sites (Figure 1) collected between 14 and 22 June 2007 were analyzed with the GIPSY software [*Lichten and Border*, 1987]. These dates encompass the dike intrusion (17–19 June) [*Poland et al.*, 2008], with data before and after the event providing information on the precision of the position estimates. Precise IGS ephemerides defined in ITRF2005 [*Altamimi et al.*, 2007] and Earth orientation parameters were held fixed, and the Niell troposphere mapping function was used [*Niell*, 1996].

[10] The positions were initially estimated independently every 4 min (i.e., a white noise model), relative to fixed sites MKPM, MLPM, and WAPM (Figure 1), which are not included in the following modeling. Sample time series are shown in Figure 2. During the intrusion, KTPM and NUPM, on opposite sides of the cracked area, rapidly diverged across the east rift zone. Maximum displacements at KTPM are larger than 10 cm in the east and 30 cm in the north component. A smaller signal is seen at the summit area site AHUP, with 6 cm of northward displacement that is consistent with deflation observed by InSAR and tilt records [*Poland et al.*, 2008]. GPS stations on the south flank (e.g., PGF3) show no discernible signal above the noise level in the white noise positions.

[11] Figure 2 also shows large position variations (e.g., at PGF3 on day 22) that are probably the result of poorly modeled tropospheric variations. The final estimation strategy used both temporal smoothing and stochastic tropo-

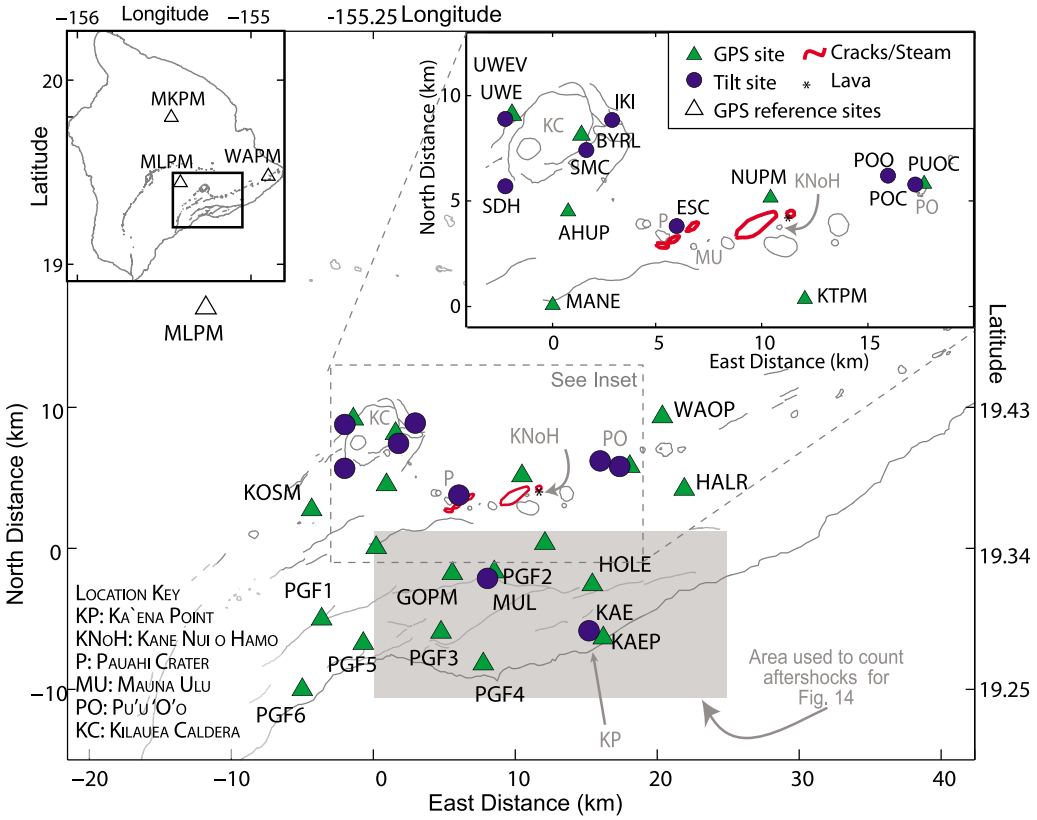

Figure 1. Reference map showing the locations of the continuously recording GPS sites (green triangles, four-letter names) and tiltmeters (blue dots, three-letter names) on Kīlauea used in this study. GPS sites MKPM, MLPM, and WAPM were held fixed for the subdaily GPS processing but not used in the source inversions. The intrusion location is marked by the cracked and steaming area (red line) and small lava flow (asterisk). The gray box marks the area used to count the aftershocks analyzed in Figure 14. The origin of the map is at the GPS site MANE (−155.273°E, 19.339°N).

sphere gradients [*Bar-Sever et al.*, 1998] for all Kīlauea sites. In addition to significantly reducing spurious displacements, adding tropospheric gradients also improves the subdaily precision of the position estimates. Details of the estimation strategy used for the GPS time series are described in greater detail by *Larson et al.* [2010].

[12] Because of the short duration of the intrusion (about 3 days), no secular velocity is removed or estimated. The maximum secular velocities on Kīlauea are ~7 cm/yr at coastal sites [*Owen et al.*, 2000b; *Miklius et al.*, 2005]. One week of accumulated displacement at these typical velocities would amount to 1.3 mm at the fastest sites over the observation period, which is well below the ambient noise level of the kinematic GPS positions.

2.2. Temporal Tilt Analysis

[13] Tiltmeter data provide accurate observations of gradients in the deformation field but can also contain significant contributions from tides and diurnal temperature variations. To better constrain tilt signals related to the intrusion, we tested three different strategies for removing the diurnal and semidiurnal variations: a linear correlation between temperature and tilt, removal of a 3 day, preintrusion, average signal from the time series, and a notch filter that removes diurnal and semidiurnal periods. Both the temperature correlation and preintrusion noise average were effective at many sites, but residual periodic signals persisted at some sites (Figure 3). We found the notch filter to be the most effective for removing the diurnal and semidiurnal signals.

[14] The notch filter is a second-order infinite impulse response time domain filter that removes frequencies of 12 ± 3.6 and 24 ± 3.6 h. The tilt signals are filtered both forward and backward in time to avoid phase shifts. Raw and notch-filtered tilt signals for site KAE are shown in Figures 3 and 4. While this method most successfully removed the diurnal noise, the onset time of the transient tilt signals remains unclear at sites with small tilts relative to the diurnal amplitude. We compared the notch filtered signal with output from cleanstrain+ [*Langbein*, 2010] and found negligible differences. Most importantly, there is no difference in the apparent onset time of the transient in the signals filtered by the notch filter versus cleanstrain+. The onset time is most important at KAE, which is a key indicator of décollement slip [*Montgomery-Brown et al.*, 2010].

[15] To objectively determine the onset time of tilting at low signal-to-noise sites, we fit a ramp function to each time series. The ramp function has a fixed amplitude, determined from preevent and postevent averages, while the onset time and duration are estimated by a Nelder-Meade simplex method [*Nelder and Mead*, 1965]. The estimated onset time at KAE is 1513 UTC (17.63 days on Figure 4), which is after the start of the intrusion at 1215 UTC (Table 1, time A),

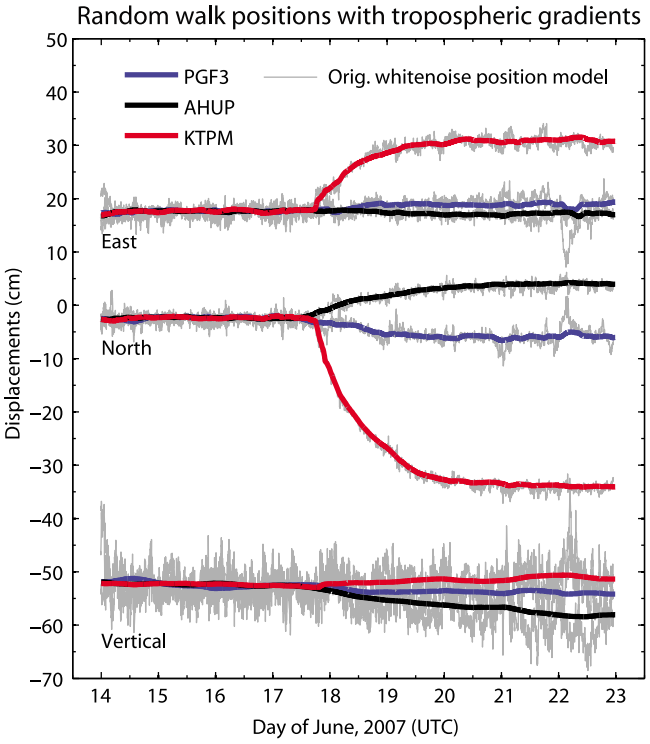

Figure 2. GPS positions of three sample sites showing improvement from initial white noise position estimates (in gray) by applying a random walk position model and estimating tropospheric gradients [from *Larson et al.*, 2010].

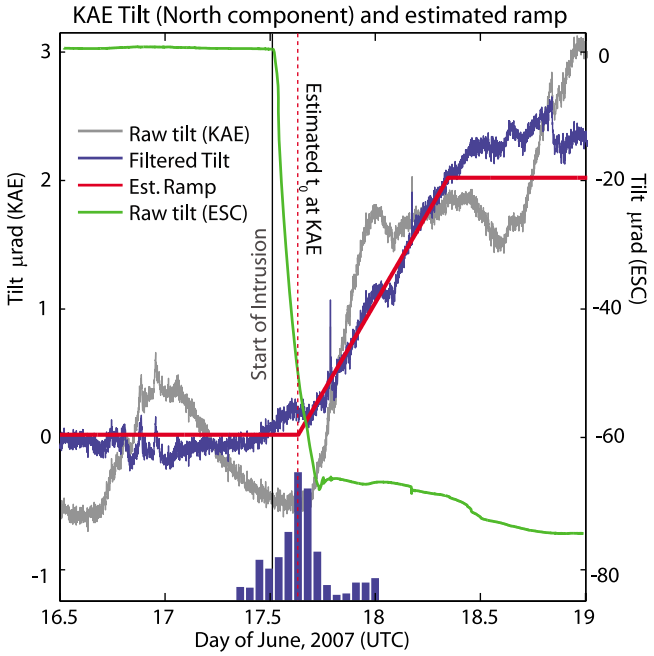

Figure 4. Raw (gray) and notch-filtered (blue) north tilt at KAE (and ESC in green for timing reference). The estimated ramp function for KAE is shown in red, with the distribution of time shifts from synthetic tests shown in the histogram below. The dashed line projects the estimated onset time (t_o) of the ramp onto the histogram; 84% of time shifts support postintrusion onset of tilting at KAE.

and the duration is 17.1 h. Applying the same method to the tilt signals filtered with temperature correlation and removal of 3 day noise averages produced estimated onset times of 1745 UTC (17.74 days) and 1725 UTC (17.72 days), respectively; both times are also after the start of the intrusion. The preferred onset time of the transient deformation at KAE is 17.63 days.

[16] To quantify the effect that the notch filtering may have on the estimated onset time of northward tilt at KAE, we generated nearly 2000 synthetic tilt signals by adding a ramp function with the approximate amplitude and duration of the tilt at KAE to a sample of background noise at KAE taken from the week before 17 June. To ensure that the true onset time of the test fell in a different part of the diurnal signal, each synthetic ramp was shifted by 10 min. Each of the synthetic signals was then notch filtered, and the onset time and duration of the ramp function were estimated by the same method as the actual data. The distribution of time shifts relative to the synthetic true onset time ($t_{true} - t_{est}$) is shown at the bottom of Figure 4. This distribution represents the possibility that the true onset of tilt at KAE is shifted due to the phase of the diurnal signal at the time the deformation began. The largest negative shift, relative to the synthetic start time was 350 min (0.24 day), while the largest positive

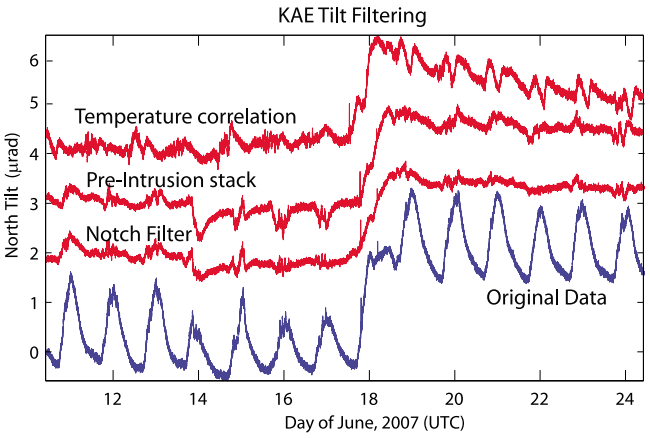

Figure 3. Raw tilt time series from the north component of KAE (blue), with the resulting filtered tilt signals from the three tested methods (offset vertically for clarity).

Table 1. Intrusion Chronology From *Poland et al.* [2008][a]

Time	Decimal Day	Event
A	17.51	Onset of seismicity Onset of tilt at ESC and UWE
B	17.73	ESC tilt flattens Down-rift concentration of seismicity
C	17.79	Summit tilt increase Onset of displacement at KTPM and NUPM
D	19.05	Slight increase in tilt at UWE Burst of seismicity
E	19.85	Summit tilt returns to inflation

[a]Times are given as the decimal day of June 2007 UTC.

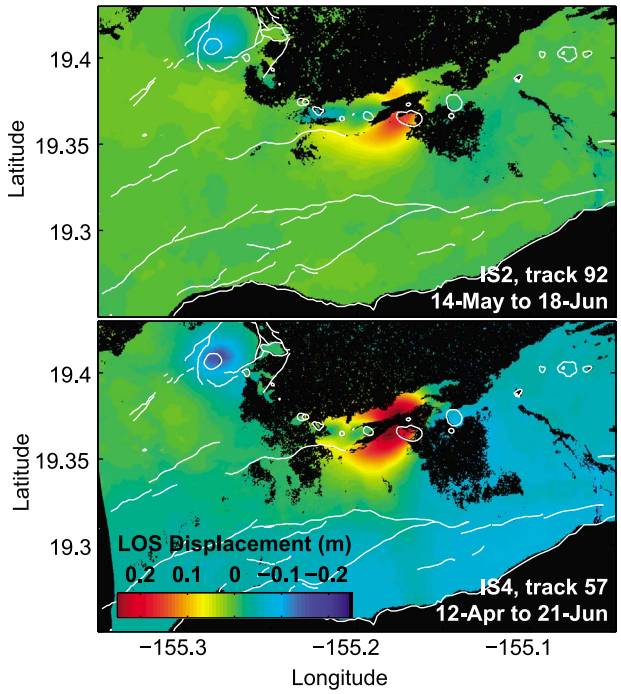

Figure 5. Two Envisat interferograms that provide increased spatial coverage at two times during the intrusion. (top) Midway through the intrusion. (bottom) After the intrusion is complete.

shift was 544 min (0.37 day). Relative to the estimated onset of northward tilting at KAE, 16% of the time shifts fall before the intrusion started, while the majority of the distribution (84%) falls after. This supports a postintrusion onset of tilting at KAE at the 84% confidence level. We conclude that it is unlikely that décollement slip, as indicated by northward tilt, preceded the intrusion event.

2.3. Interferograms

[17] Two ascending C-band (5.6 cm wavelength) Envisat interferograms provide excellent spatial coverage of the deformation at one time in the middle of the intrusion and one immediately following the complete event (Figure 5). The midevent interferogram (beam mode 2) spans 14 May at 0820 UTC to 18 June at 0822 UTC, while the interferogram (beam mode 4) of the complete event spans 12 April 0825 UTC to 21 June 0825 UTC. While ALOS data covering the complete event were used by *Montgomery-Brown et al.* [2010], the focus here is on the intrusion process and there were no midintrusion ALOS images captured. The C-band radar decorrelates in the rain forest north of the ERZ, but both images provide good coverage of the intrusion and the south flank. Both images were processed with standard methods using the GAMMA software package as described by *Montgomery-Brown et al.* [2010], and corrected for topography using a 30 m digital elevation model from the Shuttle Radar Topography Mission [*Farr and Kobrick*, 2000].

[18] Both images show lobes of line-of-sight (LOS) uplift adjacent to the rift zone, and subsidence in the summit area. When used in the inversions, both images are spatially subsampled with a quadtree algorithm [*Welstead*, 1999] with a variance tolerance of 0.01 m^2 within each quadrant. The covariance matrices for the InSAR data are assumed to be diagonal with the value for each quadrant being the variance tolerance (0.01 m^2).

3. Spatiotemporal Model

3.1. Methods

[19] In this section we analyze the spatiotemporal evolution of the June 2007 events with a simple model of the dike intrusion and décollement slip. The data, $\mathbf{d}(\mathbf{t_k})$, used in the inversion are the displacements and tilts at each epoch. Displacements are computed as the difference between the observed position, $\mathbf{x}(\mathbf{t_k})$, at each time step, t_k, and the previous position, $\mathbf{x}(\mathbf{t_{k-1}})$, as

$$\mathbf{d}(\mathbf{t_k}) = \mathbf{x}(\mathbf{t_k}) - \mathbf{x}(\mathbf{t_{k-1}}). \quad (1)$$

Offsets in the tilt data are computed in the same way, as the difference between the observed tilt and the tilt at the previous time step. We are limited to using the continuously recording instruments which include 19 GPS sites (m = 19) and 9 tiltmeters (n = 9). In equation (2), $\mathbf{d}$, is therefore a 75-element vector containing $3m$ components of GPS observations and $2n$ components of tilt observations used to invert for the model parameters at each epoch.

[20] The fixed source geometry used here includes two planar en echelon dike segments and two spherical magma reservoirs (one at the summit and one under Pu'u 'Ō'ō), and a décollement at 8 km depth. This source geometry was chosen through an initial Monte Carlo optimization for a uniform dislocation, and further testing of more complex distributed-opening intrusion geometries using a full compliment of continuous GPS, campaign GPS, tilt and InSAR data of *Montgomery-Brown et al.* [2010]. Each en echelon dike segment is nearly vertical and subdivided into 0.5 km patches. The décollement extends across the south flank at a depth of 8 km, and is subdivided into a 10 by 5 grid of 4 km by 4 km subfaults. Despite its simplicity, the Mogi source provided a satisfactory fit to the GPS, tilt and spatially dense InSAR data that recorded the final deformation field studied by *Montgomery-Brown et al.* [2010]. More complex models (e.g., ellipsoidal shape or heterogeneous host rock properties) are likely not resolvable with such limited spatial coverage and the Mogi model satisfies the current summit data sufficiently in this analysis such that the dike models of interest are not biased by summit deformation.

[21] Independent inversions determine the best fitting model at each 4 min epoch by minimizing the L2 norm of the weighted residual vector with a spatially smoothed nonnegative least squares algorithm. In the inversions, the GPS and tilt observations at each epoch are weighted by the inverse square root of their respective variances. The Kalman filter-based Network Inversion Filter [*Segall and Matthews*, 1997] has often been used for modeling gradually evolving geodetic signals [*Miyazaki et al.*, 2003; *Murray and Segall*, 2005; *Desmarais and Segall*, 2007], but in this case the sharp tilts (e.g., ESC, Figure 10) and rapidly changing GPS positions (e.g., NUPM and KTPM, Figure 9) make the standard implementation of the Network Inversion Filter less than ideal for this application. *Fukuda and Johnson* [2008] outline a fully Bayesian filter method that allows for

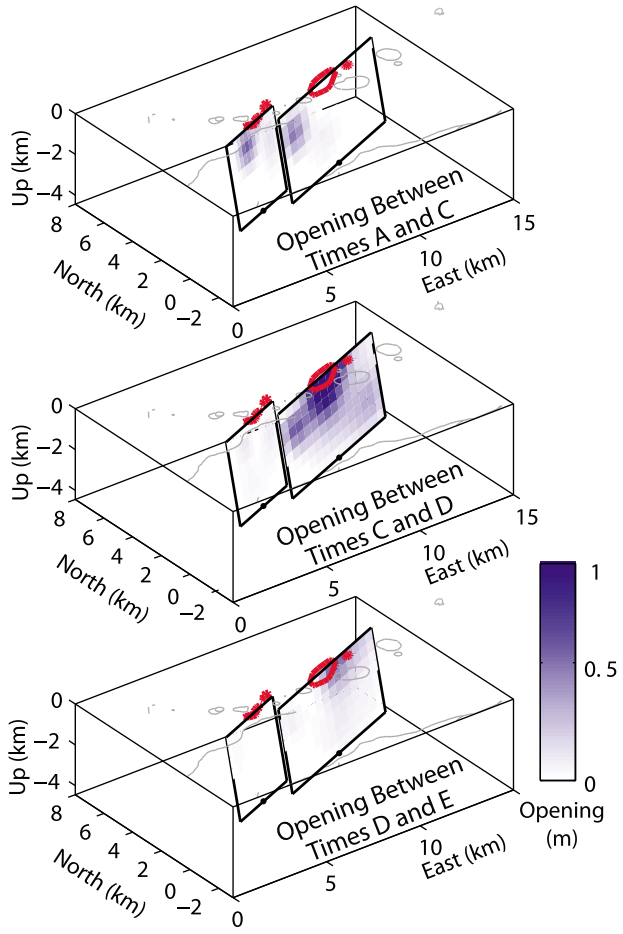

Figure 6. Distributed opening on both dike segments during time periods A–E defined in Table 1. Color intensity indicates how much opening occurred on that patch of the dike. Red outlines mark the extent of ground cracking observed after the intrusion.

abrupt changes. Additionally, since the GPS data have been temporally smoothed as part of the processing, the resulting model parameters are relatively smooth.

[22] Spatial smoothing is implemented as pseudo observations by

$$\begin{bmatrix} \mathbf{d_{GPS}} \\ \mathbf{d_{tilt}} \\ \mathbf{0} \end{bmatrix} = \begin{bmatrix} \mathbf{G} \\ \nabla^2 \end{bmatrix} \mathbf{m} + \epsilon, \qquad (2)$$

where $\mathbf{d_{GPS}}$ and $\mathbf{d_{tilt}}$ are vectors of displacements and tilts computed from equation (1), $\mathbf{m}$, is a vector of the model parameters to be estimated, and $\mathbf{G}$ is a matrix of Green's functions relating the two. ∇^2 is a finite difference Laplacian smoothing operator, and ϵ are the remaining errors. Green's functions, $\mathbf{G}$, relating the deformation of each source to the data are computed from *Okada* [1985] for each rectangular dike patch and from *Mogi* [1958] for each point source approximating a magma reservoir. Both of these models assume a homogeneous, isotropic, linearly elastic half-space. More complex models accounting for effects such as viscoelasticity are not relevant to the timescale of this study (a few days). We assume a Poisson's ratio of 0.25 and a shear modulus of 3×10^{10} Pa.

[23] The weight put on smoothing the model versus fitting the data is determined by the L curve criteria [*Hansen*, 1992] in which the optimal weight produces the smoothest model with a minimal increase in residual norm. Details of the L curve method and its application to this type of geodetic inversion are given by *Montgomery-Brown et al.* [2010]. Since the number of data and model parameters remains the same throughout the time-dependent modeling, the smoothing weight is determined a priori for a model of the cumulative deformation and held fixed during the time-dependent inversion. As a result, models early in the time series when the signal-to-noise ratios are low may be undersmoothed. Smoothing parameters varying between 10^3 and 10^9 were tested for the dikes and décollement, and the model smoothness and residual norm were compared for each combination.

[24] We solve equation (2) for the amount of opening on each patch of both dikes, the volume change of the Mogi sources at the summit and Pu'u 'Ō'ō, and slip on the décollement such that $\mathbf{m} = [\mathbf{m_{op1}}\ \mathbf{m_{op2}}\ \mathbf{m_{sumV}}\ \mathbf{m_{PuuOoV}}\ \mathbf{m_{decol}}]^{\mathbf{T}}$. For the purposes of the positivity constraints in the least squares algorithm, opening of the dike segments, deflation of the summit magma reservoir and Pu'u 'Ō'ō, and seaward décollement slip are considered positive. Enforcing positivity constraints on dike opening has the effect of preventing a section of the dike from opening and then subsequently closing, while enforcing the constraints on décollement slip prevents northward slip, which is geologically infeasible and is not observed.

3.2. Results

[25] We display the spatiotemporal model in two ways: (1) showing the distribution of dike opening during three time periods to highlight the spatial evolution of the dike opening (Figure 6) and (2) as a time series of total dike volume at each epoch to highlight the temporal change of dike opening (Figure 7). Figures 6 and 7 show that the June 2007 intrusion started on the western dike segment just after noon on 17 June 2007 UTC (17.51 days, time A) near Pauahi Crater, which is under the mapped western crack area [*Montgomery-Brown et al.*, 2010] (Figure 6), and that this segment continued to inflate for several hours. By 17.79 days (time C), inflation moved to the eastern dike segment near Makaopuhi Crater and under the eastern cracked and steaming area. The eastern segment continued to inflate for nearly 2 days until the end of 19 June (time E).

[26] The summit magma reservoir exhibits two accelerations in volume loss coinciding with the onset of dike intrusion on each segment (Figure 7). These rate increases of about 3–5 m^3/epoch occur at time A and at time B (Figure 7 and Table 1). The volume-loss rate slows to about half of the local maximum rate within a few hours, with a rapid decrease midway between times C and D. After the two accelerations, and one small acceleration early on day 19, the change in volume rate slows significantly. The return to inflation observed at summit tiltmeters (e.g., UWEV at time E) is not seen in the model in Figure 7 because inflation was not allowed by the nonnegative least squares algorithm used in this inversion.

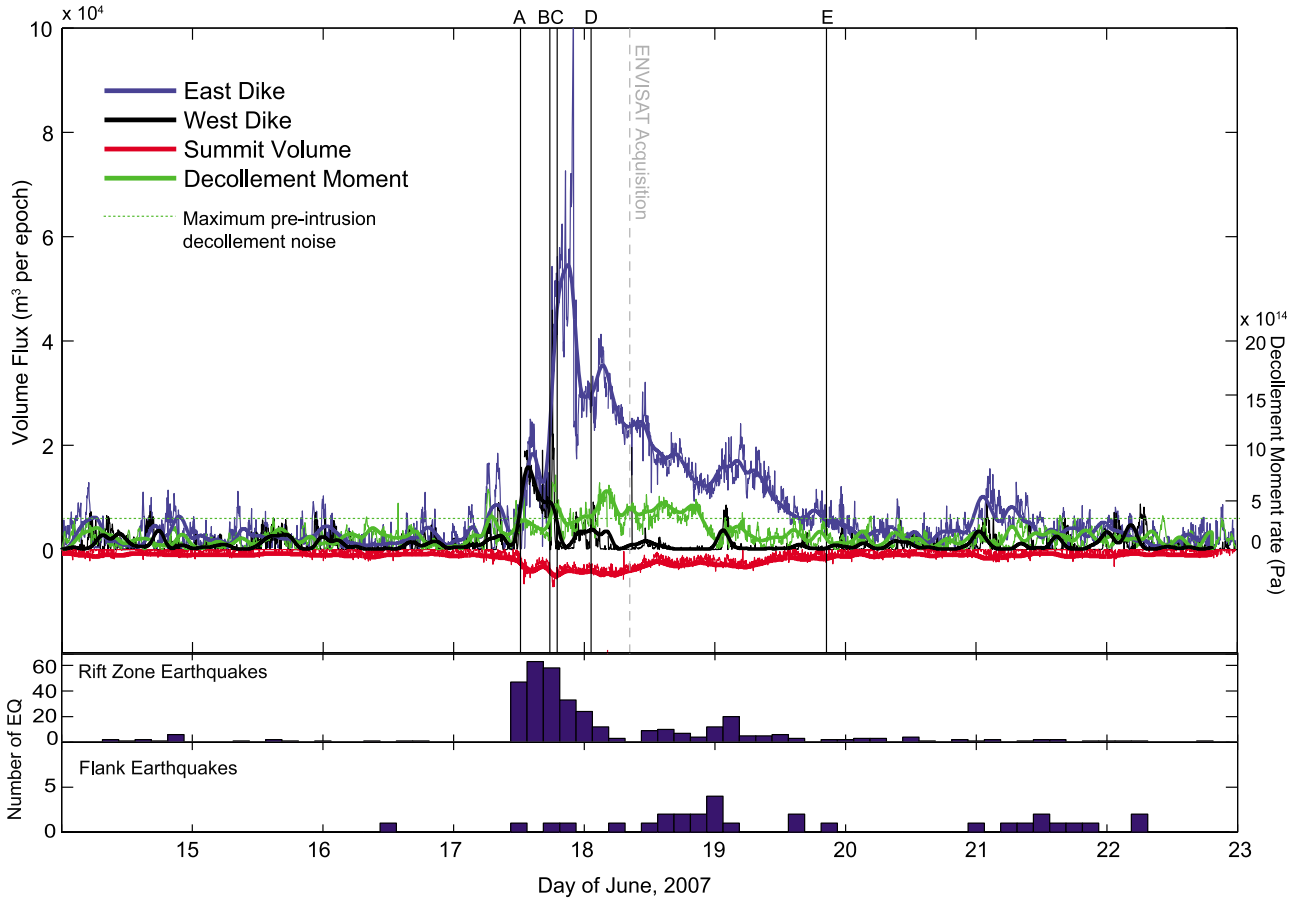

Figure 7. A comparison of the time-dependent rates of west dike volume change (black), east dike volume change (blue), summit volume change (red), and décollement moment rate (green). For clarity, each signal has been overlain with the same signal smoothed with a 4 h moving window. Histograms show hourly counts of catalog earthquakes in the rift zone and the south flank.

[27] Modeled décollement slip rates are noisy due to a low signal-to-noise ratio; we compute the maximum of the décollement slip rates from the preintrusion time period as a measure of the error in the modeled signal. The modeled décollement slip exceeded maximum preintrusion noise levels at ~17.8 days, and remained elevated until ~18.9 days (Figure 7). Elevated slip rates following the onset of dike opening suggest that the décollement slip began after the intrusion.

[28] Comparing the data and model predictions both in map view (Figure 8) and time series (Figures 9 and 10) show that overall the data are well fit through time by a combination of dike opening and décollement slip. Near-field displacement (Figure 9, e.g., KTPM and NUPM) and tilt time series (Figure 10, e.g., ESC) are reasonably well fit regardless of whether or not décollement slip is included. Specifically, this agreement is seen in the predicted and observed timing of the sharp southward tilt at ESC (Figure 10) and of the extension across the rift zone seen at GPS sites KTPM and NUPM (Figure 9). At all summit sites, the temporal shapes of the time series are well fit, although the magnitudes differ (e.g., UWE and UWEV). The magnitude misfits likely arise because the simple Mogi source is inadequate for modeling the complex summit magma reservoir, but are sufficient enough not to bias the rift zone models.

[29] The observed subsidence near the coast and across the south flank is only predicted by models that include décollement slip; uplift is predicted by dike-only models. The fit to the northward tilt at KAE is also significantly improved when including décollement slip, since very small southward tilts are predicted by dike-only models (Figure 10). Without décollement slip, a notable misfit is seen beginning at about 18.2 days at GPS sites PGF1, PGF5 and PGF6, which are shown as the sum of the three due to their low signal-to-noise ratio (Figure 9).

[30] To better understand the spatiotemporal resolution of the data, we conducted tests in which opening is restricted to individual dike segments. If dike opening is restricted to the western segment, significant misfits appear at KTPM and NUPM starting at about 17.79 days (time C). In this restricted model, the predicted displacements at these intrusion-spanning GPS sites are never able to attain magnitudes close to those observed. Misfits are also apparent in the predicted tilts at ESC tiltmeter. This model predicts that ESC would continue to tilt significantly southward after 17.75 days, while the observed tilts stabilize after this time (Figure 10).

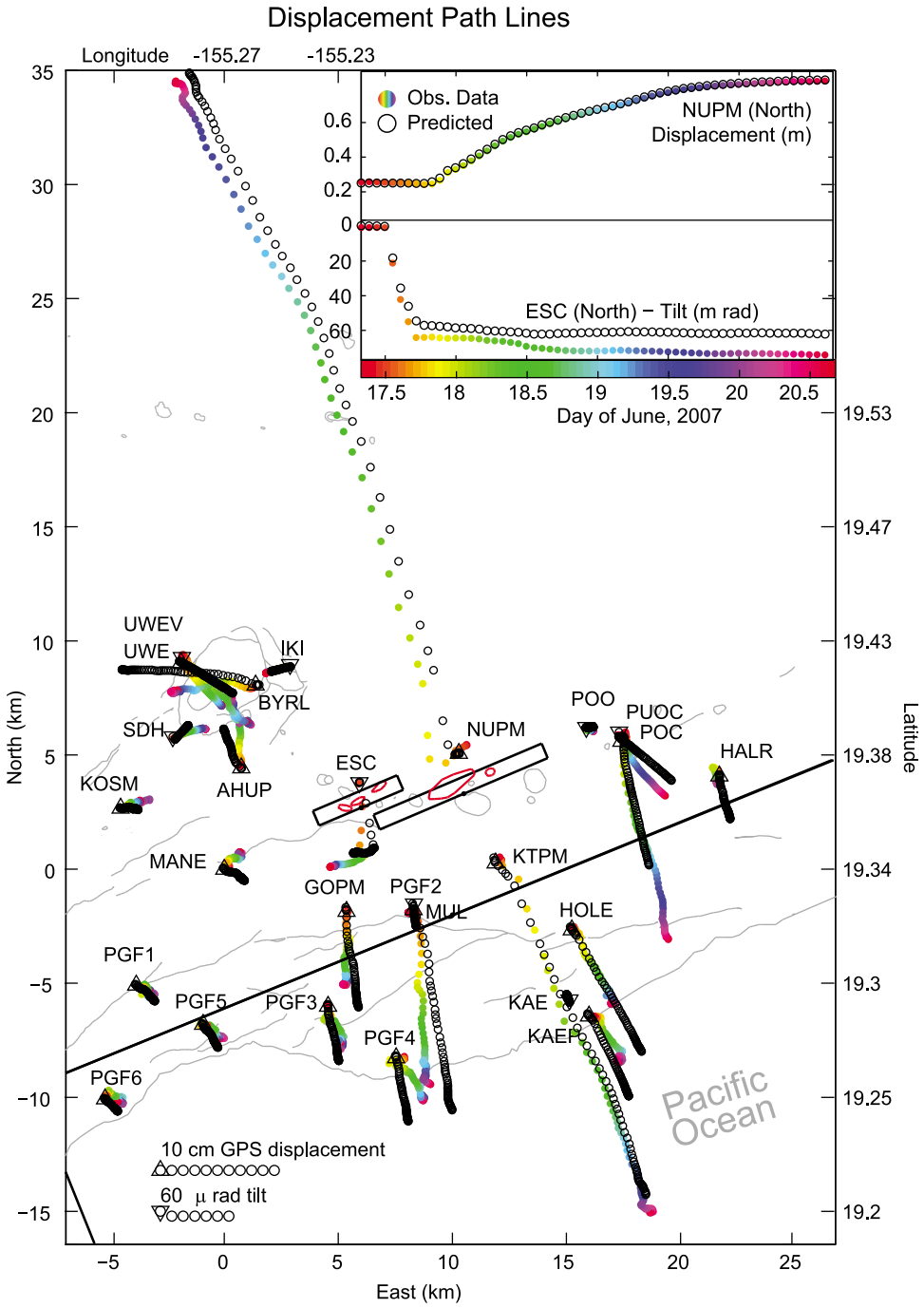

Figure 8. GPS displacements and tilts (every 20th epoch) shown as path lines. Continuous GPS site locations and tilt site locations are shown by triangles and inverted triangles, respectively. Black dots are observed positions and tilts, while colored dots are the respective positions and tilts predicted by the model. The colored markers representing displacements on the map match the colors on the time series inset.

Also at ESC, this model predicts eastward tilts would continue for the duration of the event, despite significant westward tilts in the observed data after 18.4 days.

[31] Conversely, if dike opening is restricted to the eastern dike segment, the majority of the GPS data are well fit. However, the initial sharp, 64 μrad drop in tilt at ESC at the beginning of the intrusion is completely missing from the predicted tilts, as is the eastward tilt at ESC between 17.6 and 18.4 days. Reasonable fits to the data can be obtained by allowing dike opening on only the western segment until time C, followed by opening on the eastern segment from time C until the end of the event. The most likely scenario is that both segments are active between 17.6 and 18.4 days.

[32] We can perform a similar analysis to determine when décollement slip is required by the data. As discussed in the introduction, it is difficult to separate southward

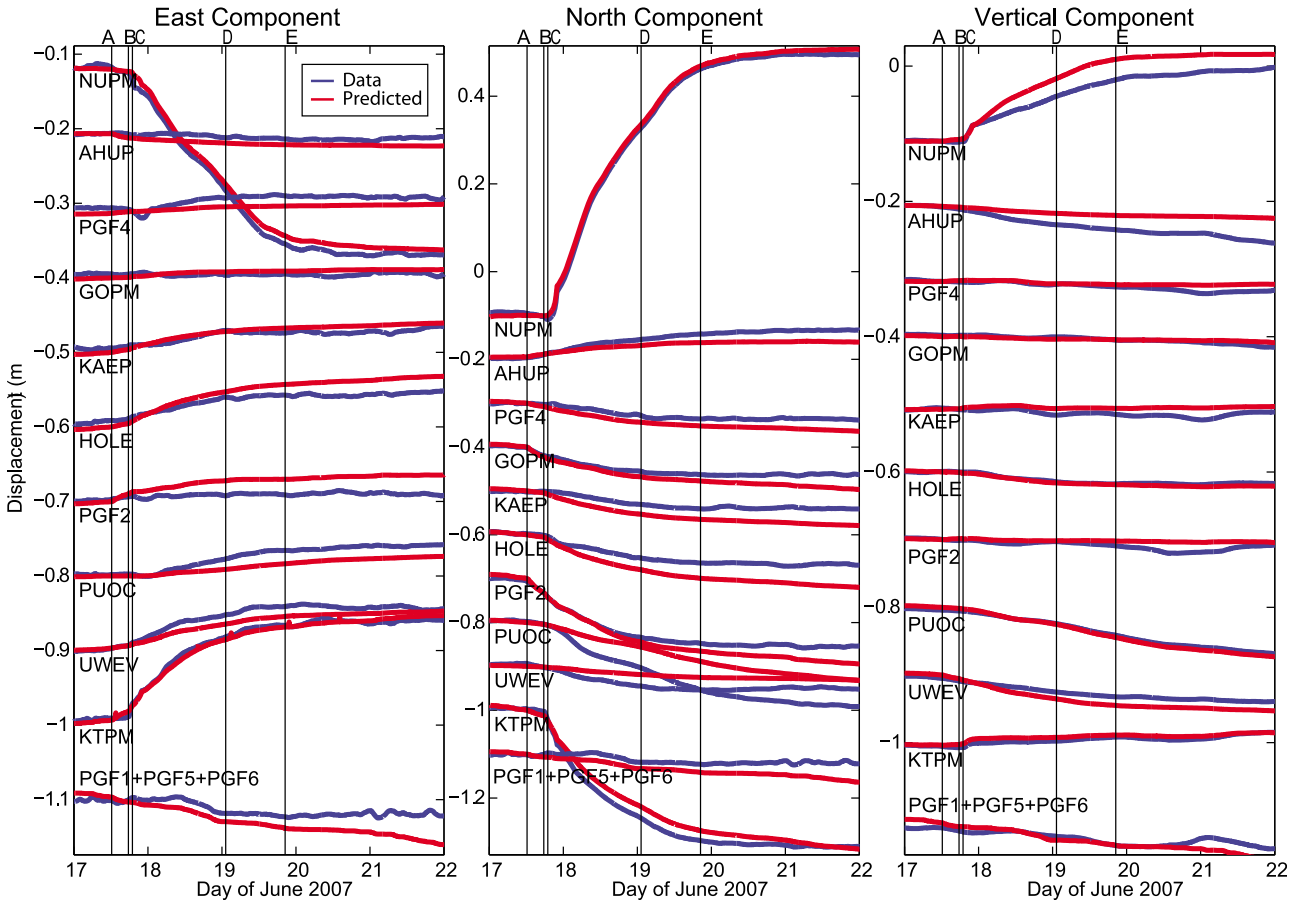

Figure 9. Selected observed GPS displacements (blue) and predicted displacements from two models. For clarity, sites with redundant information are not displayed. Predicted displacements in red were produced by a model that estimated magma volumes (a pair of en echelon dike segments and magma reservoirs beneath both the summit and Pu'u 'Ō'ō) and décollement slip. Vertical lines indicate the times A–E in Table 1.

displacements induced by dike opening from those induced by décollement slip since few GPS or tilt stations are located where décollement slip dominates the observations. Two notable indicators include northward tilt at KAE and displacements at GPS sites PGF1, PGF5 and PGF6. These sites, however, do not begin to move at the same time. By restricting when the décollement is allowed to slip, we can analyze the misfits to determine when slip is required by the data.

[33] We first limit the décollement slip to occur only after the onset of northward tilting at KAE (17.63 days, Figure 4). The fits to KAE and GPS sites PGF1, PGF5 and PGF6 are satisfactory, suggesting that décollement slip is not required by the data before this point. However, restricting décollement slip to occur only after those GPS sites begin to move significantly at 18.2 days delays the predicted onset of northward tilting at KAE by about 0.6 day.

[34] To further analyze the timing of the décollement slip, we examine the temporal evolution of slip on two model patches, one offshore of Ka'ena Point (near the KAEP GPS site and KAE tiltmeter) and the other offshore of the southwest flank (Figure 11). The slip history of two representative fault patches shows that the décollement nearer KAE begins to slip earlier than a similar fault patch farther southwest.

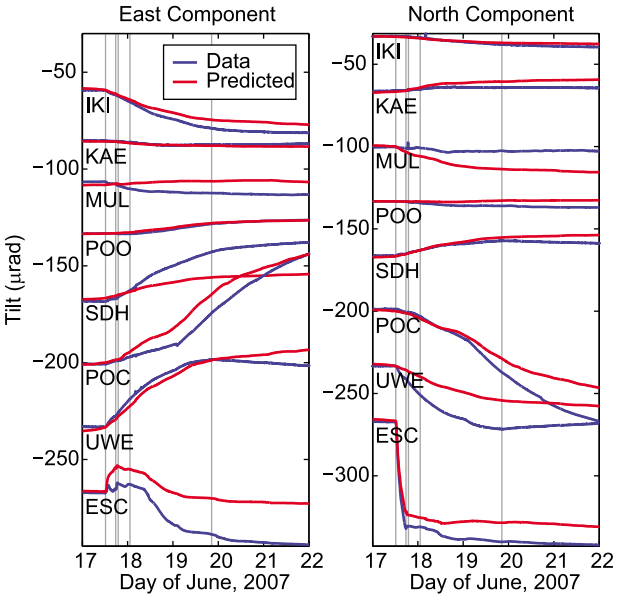

Figure 10. Selected observed tilts (blue) and predicted tilts (red) from the same model as in Figure 9. Vertical lines indicate the times A–E in Table 1.

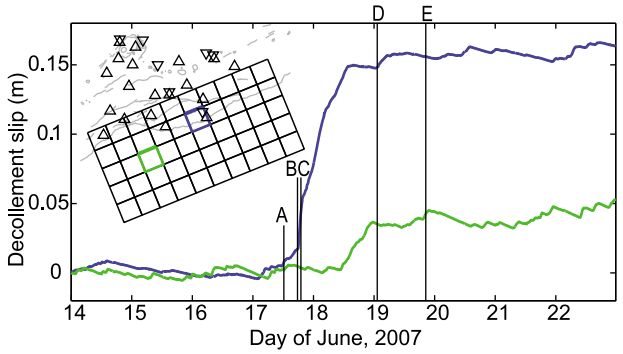

Figure 11. Slip history of two representative fault patches on the décollement. Vertical bars represent times A–E in Table 1.

Although the signal is noisy and dependent on few stations, this observation suggests that décollement slip may have begun near KAE and migrated southwestward during the slip event. This conclusion should be accepted with caution since this inferred slip migration is highly dependent on one tilt station (KAE) and a few GPS stations(PGF1, PGF5, and PGF6) with low signal-to-noise ratio. The duration of slip on each of these two fault patches individually is shorter than the typical ~2 day duration of the slow slip events on Kīlauea's south flank [*Montgomery-Brown et al.*, 2009]. Together, however, the duration of the complete event, from the earliest slip on a single patch to the latest slip on a single patch, is more consistent with the length of a typical slow slip event (Figures 7 and 11).

4. Midintrusion and Postintrusion Interferograms

[35] In this section we perform two inversions including Envisat InSAR data and compare the volumes at the relevant times in the time-dependent model above. The two Envisat interferograms provide denser spatial observations than GPS and tilt alone and can help produce the best constrained model of the cumulative deformation up to the time of the second image capture in each interferogram. Inversions are conducted of the Envisat data including cumulative GPS displacements and ground tilt up to the time of the second Envisat image in each interferogram. The model is the same as in section 3 and includes two en echelon dike segments, two magma reservoirs, and décollement slip (Figure 12). The inversions are also accomplished with the same method using a nonnegative least squares algorithm with Laplacian spatial smoothing constraint.

[36] The first inversion is used to analyze the cumulative deformation up to the midintrusion Envisat image capture,

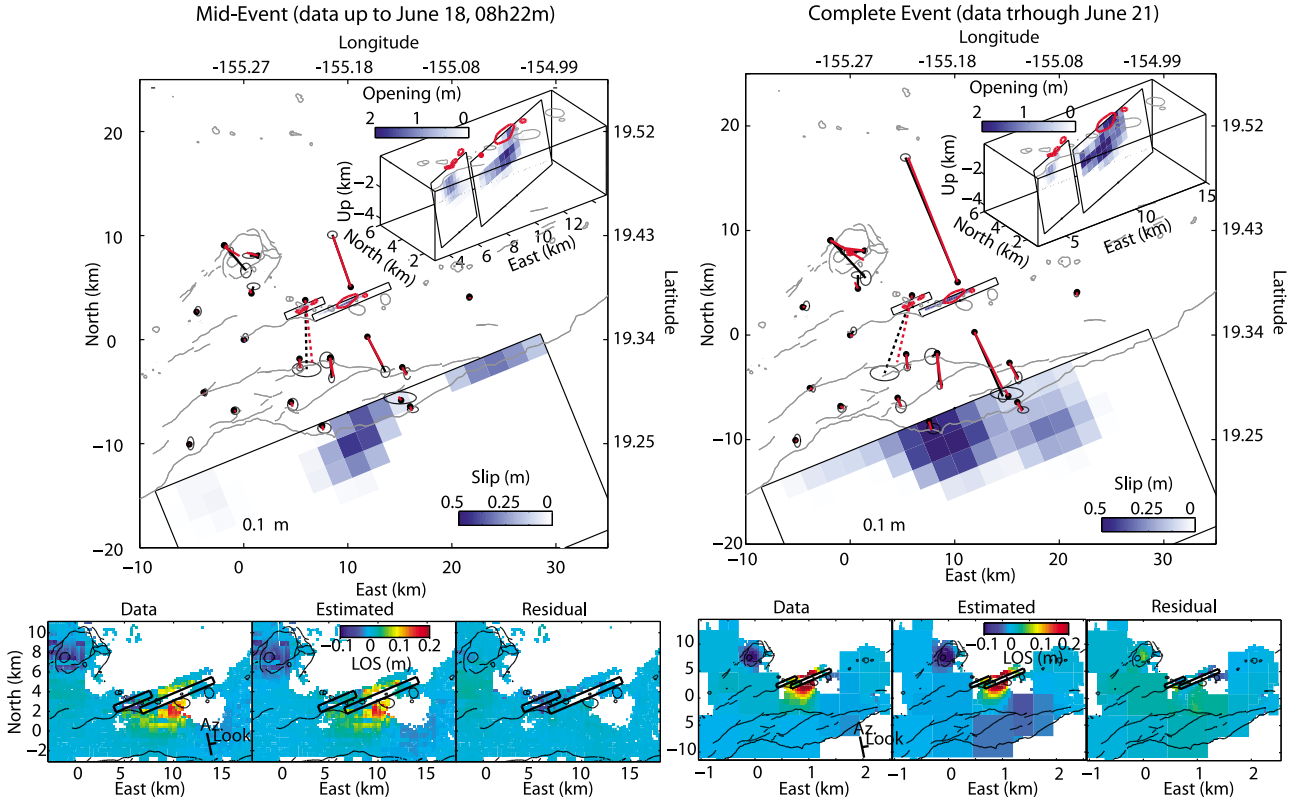

Figure 12. Comparison of models of the two Envisat interferograms on the same color scale. The models also include continuous GPS and ground tilt data up to the time of their respective Envisat image. GPS displacements are indicated by solid vectors, and tilts are shown with dotted vectors. Dike opening and décollement slip magnitudes are indicated by the intensity of the blue color, with a maximum opening of 2 m and a maximum décollement slip of 0.25 m.

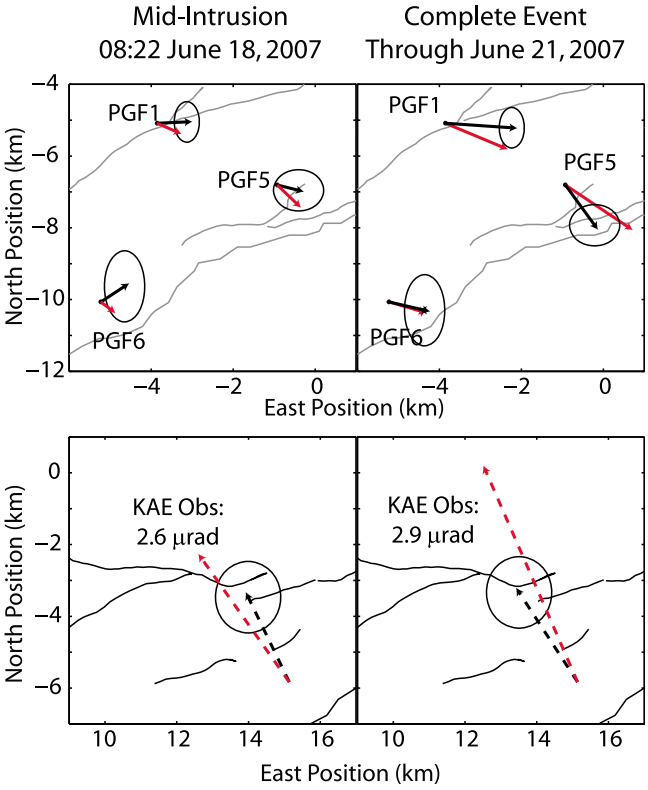

Figure 13. Comparison of observed (black) and modeled (red) GPS (top) and tilt (bottom) data in map view at the time of the two Envisat images. Error ellipses show 95% confidence intervals.

and includes GPS displacements and tilt up to 0824 UTC on 18 June 2007 (between times C and D, Figure 7), the closest GPS epoch to the image capture time. The second inversion uses the postintrusion Envisat interferogram with the cumulative GPS displacements and tilt up to 21 June 2007 and provides a direct comparison of the midintrusion dike opening and décollement slip to that of the complete intrusion. In both inversions, each data set is weighted by the inverse of the square root of its variance.

[37] InSAR displacements, cumulative GPS displacements, and most tilts up to the Envisat capture at 822 UTC on 18 June are reasonably well fit by deformation due only to the dike intrusion. This is not the case for the entire event [See also *Montgomery-Brown et al.*, 2010]. Negligible deformation was observed at PGF1, PGF5, and PGF6 up to the time of the first InSAR image (Figure 13). KAE, however, had accumulated most of the observed northward tilt by the time of the midintrusion Envisat capture (Figure 13), and some décollement slip concentrated close to Ka'ena Point is required to satisfy this observation (Figure 12). Inverting for the same deformation sources using the second Envisat image on 21 June plus GPS and tilt data up to that time, however, requires décollement slip to be spread across the south flank. This again suggests that slip may have migrated westward during the intrusion. Although the volumes in the time-dependent model were not constrained by the InSAR data, the volumes determined from these two snapshot models are consistent with cumulative volumes obtained in the time-dependent models at these epochs.

5. Flank Aftershocks

[38] The décollement slip that accompanies the June 2007 dike intrusion is associated with a small number of earthquakes, similar to the coshock and aftershock sequences observed during previous slow slip events [*Segall et al.*, 2006; *Wolfe et al.*, 2007]. If we accept the relationship between stress rate and seismicity given by *Dieterich* [1994], we can use this aftershock sequence to make an independent estimate of the slow slip onset time.

[39] *Segall et al.* [2006] and *Montgomery-Brown et al.* [2009] showed that swarms of earthquakes on the south flank of Kīlauea Volcano that accompany slow slip events were consistent with the temporal evolution of seismicity using *Dieterich*'s [1994] seismicity rate theory. According to this model, the earthquake rate, R, can be computed from

$$R = \frac{dN}{dt} = \frac{r}{\gamma \dot{\tau}_r}, \tag{3}$$

where N is the number of earthquakes, t is time, and γ, a seismicity state variable, that evolves with shear stress, τ, and normal stress, σ, as

$$d\gamma = \frac{1}{a\sigma}[dt - \gamma d\tau + \gamma(\tau/\sigma - a)d\sigma]. \tag{4}$$

In this case, the cumulative number of expected earthquakes, N, is computed for each event from a ramp function estimate of slip, and hence stress, as in equation 3 of *Segall et al.* [2006].

[40] The south flank earthquake rate did not increase sufficiently above background levels during the 2007 events to invert for the onset time of the stress rate increase. Instead, forward predictions of seismicity rates are analyzed while varying the onset time of the inferred slow slip. The other required parameters are computed or assumed to be similar to previous events. A typical slip duration of 1.5 days is consistent with the duration found in section 3. From previous slow slip events, it is assumed that the ratio of background stressing rate to event stressing rate is similar to previous slow slip events at ~15, and the aftershock decay time is about 7 days [*Montgomery-Brown et al.*, 2009]. It is plausible that stresses related to the dike intrusion might add to the stressing rates, but seismicity rates did not increase in the area of the slow slip swarm following previous intrusions in 1997 and 1999. Thus, it is also presumed that the intrusion did not increase the stressing rate on the décollement enough to influence the seismicity rates because seismicity in this area has not increased following recent prior intrusions. The background rate of 1.5 earthquakes per day is determined from the preevent rate from the first 2 weeks of June 2007. Onset times are chosen based on relevant geodetic events and include (1) the onset of the intrusion at 17.51 days, (2) the onset of décollement slip as indicated by northward tilting at KAE at 17.63 days, and (3) the onset of displacements at the southwest flank GPS sites PGF1, PGF5 and PGF6 at 18.2 days.

[41] Misfits between the observed and predicted earthquake rates (Figure 14) are indistinguishable for start times

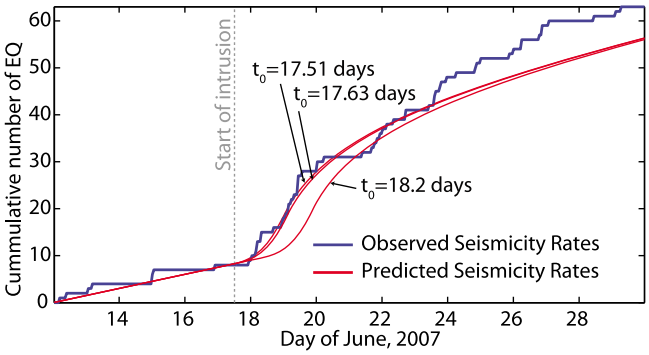

Figure 14. Cumulative seismicity on the south flank of Kīlauea volcano (earthquakes within the box 0.5 to 25 km east-west and 1 to −10 km north-south, Figure 1) are compared with seismicity rates computed with varying onset times and typical slip durations, stressing rates, and aftershock decay times. Onset times corresponding to the start of the intrusion (17.51 days), and the start of northward tilt at KAE (17.63 days) predict misfits to the observed seismicity rates that are indistinguishable from each other.

corresponding to the onset of the intrusion (17.51 days), and the onset of northward tilting at KAE (17.63 days). The onset time corresponding to the displacements at the southwest flank GPS sites (18.2 days) poorly fit the observed earthquake time series, and varying the other model parameters could not suitably improve the fit with this onset time. Although there are too few earthquakes to allow for an independent estimate of the time that slow slip initiated, the "coshock" and aftershock sequence could have been produced by a stress increase resulting from the onset of slow slip as indicated by northward tilting at KAE.

6. Discussion and Conclusions

[42] The June 2007 Kīlauea intrusion began with ~6 h of inflation of the western dike segment near Pauahi Crater, then shifted down rift to a second segment near Makaopuhi Crater, which inflated for ~2 days. The summit magma reservoir deflated throughout the intrusion with rate increases coinciding with the pulses of dike inflation. Décollement slip began after the onset of the dike intrusion near the time when the second dike segment began opening and may have migrated toward the west over ~2 days.

[43] The June 2007 intrusion migrated about 7 km down rift from the western segment to the eastern segment. The small amount of magma erupted at the surface on 19 June occurred near the down-rift tip of the dike and appears to have erupted after the majority of the dike volume was emplaced. The shift in the location of dike opening from the first to the second segment corresponds to a down-rift migration in shallow rift zone earthquakes.

[44] While the opening propagated down rift from the western segment to the eastern segment, the inversions reveal little migration of opening within either segment. In other words, the opening within a segment, specifically the western segment, appears to occur simultaneously across the whole segment. However, lateral resolution on individual dike segments is limited by the few near-field observations, so propagation within a segment is likely not resolvable. While it is assumed that magma is transported from the central magma reservoir out to the rift zones at some depth, the geodetic data do not require any opening of the deep rift zone. This suggests that the process of moving magma out to the rifts either produces no deformation, or that the deformation occurring is too small or too deep to be resolved. The geodetic data are also unable to resolve whether the two dike segments could have merged at depth. However, activity in the upper east rift zone during this event in the form of small earthquakes along the surface trace of the rift zone suggest that other parts of Kīlauea's plumbing system were participating in the event. One common interpretation of Kīlauea's plumbing system involves a persistent conduit leading from the central reservoir out into the rift zone supplying the continuing eruptions at Pu'u 'O'o [*Swanson et al.*, 1976; *Cervelli et al.*, 2003]. An open conduit would not necessarily deform while transferring magma into the new dikes, so if this model is applicable, the deep transfer of magma may not be observed with geodetic instruments. Integrating a variety of other geophysical data in the future will perhaps improve our interpretation of magma plumbing systems.

[45] The June 2007 sequence of events is unique because it is the first observation of an intrusion and concurrent slow slip event on Kīlauea. Based on the recurrence of past slow slip events, *Brooks et al.* [2006] suggested that a slow slip event on Kīlauea's south flank might occur in March 2007. The event had not occurred by the time of the June 2007 intrusion. *Brooks et al.* [2008] further suggest, based on the timing of the displacements at the southwest flank GPS sites, that the intrusion may have triggered the slow slip event. Indeed, the temporal relationship established in this current analysis supports the intrusion preceding the flank slip, suggesting that the intrusion triggered the slow slip. To the extent that the timing of tilt at KAE tiltmeter is reliable, the slow slip may have coincided with the onset of inflation at the second (eastern) segment of the dike (Figures 7 and 11).

[46] We have shown that the temporal relationship between the dike opening and the décollement slip does indeed suggest that the dike opening triggered the décollement slip. However, the flank has slipped before without being triggered by dike intrusion [e.g., *Cervelli et al.*, 2002b; *Brooks et al.*, 2006; *Montgomery-Brown et al.*, 2009]. Conversely, several intrusions have been recorded without measured transient flank deformation [e.g., *Owen et al.*, 2000a; *Cervelli et al.*, 2002a; *Desmarais and Segall*, 2007]. It should be noted that *Dvorak et al.* [1986] showed that the south flank seismicity rate significantly increases immediately following intrusions, primarily in the area between the rift zone and the palis. While deformation resulting from the increased seismicity may not have been observed, it can be assumed that they result from some small flank slip. Only four intrusions and ten slow slip events have occurred on Kīlauea in the era of continuous GPS since 1996, so the likelihood that both would have occurred on the same day is relatively small.

[47] *Brooks et al.* [2008] indicated that the dike intrusion and the accumulated secular deformation since the last slow slip event in 2005 contributed equally to the Coulomb failure stress on the décollement. The secular model used by *Cayol et al.* [2000] is based on data prior to the 1983 ERZ intrusion, deformation is accommodated by rift dilation

from the near surface to 9 km deep and décollement slip limited to an area very close to the rift zones. In contrast, *Owen et al.* [2000b] used more recent (post 1990) GPS velocities that are more similar to contemporary rates. They show that flank deformation is accommodated both by deep dike opening (between 3 and 10 km below the surface), and décollement slip that extends from the rift zone to several kilometers offshore. *Owen et al.* [2000b] show that slip extends significantly south of the Hilina fault system with 95% confidence, but resolution of the offshore extent is limited when using only onshore geodetic data. Offshore geodetic data [*Phillips et al.*, 2008] support offshore fault slip extending at least 15 km southward from the coast. The variability of these models indicates that the rate at which the décollement accumulates stress depends on the time period of study. Additionally, we can presume that these studies averaged over any slow slip events because the data did not have the temporal resolution to identify short-term transients. Thus, further work is needed to determine where slip is occurring on the décollement between slow slip events and what are the physical properties of the décollement surface.

[48] Based on the current data, we cannot rule out a scenario in which the first pulse of the dike intrusion occurs and triggers slow slip. The slow slip in turn facilitates additional dike opening. A scenario like this accounts for the delayed décollement slip as well as the multiple pulses of the intrusion. *Dieterich* [1988] showed that the rift zone expansion and southward flank motion are inherently intertwined. The close temporal relationship between the 2007 intrusion and the flank slip suggests that this interaction can occur on short timescales if the right conditions exist. Continued monitoring of Kīlauea and other volcanoes with a variety of techniques (e.g., geodetic, seismic, gravity, etc.) and the joint interpretation of these data sets will greatly help to further our understanding of volcano dynamics and how a volcano's magmatic system interacts with its flanks.

[49] **Acknowledgments.** The authors would like to acknowledge our ongoing collaborations with the Hawaiian Volcano Observatory and the University of Hawaii. This work was supported by NSF research grant EAR-0537920 and a SGER grant. E.M.B. was also supported by a NASA Earth Systems Science Fellowship. We would also like to thank Associate Editor Michael P. Ryan and two anonymous reviewers for their thoughtful comments that greatly improved the initial manuscript.

References

Altamimi, Z., X. Collilieux, J. Legrand, B. Garayt, and C. Boucher (2007), ITRF2005: A new release of the International Terrestrial Reference Frame based on time series of station positions and Earth orientation parameters, *J. Geophys. Res.*, *112*, B09401, doi:10.1029/2007JB004949.

Bar-Sever, Y., P. Kroger, and J. Borjesson (1998), Estimating horizontal gradients of tropospheric path delay with a single GPS receiver, *J. Geophys. Res.*, *103*(B3), 5019–5035, doi:10.1029/97JB03534.

Bonaccorso, A., M. Aloisi, and M. Mattia (2002), Dike emplacement forerunning the Etna July 2001 eruption modeled through continuous tilt and GPS data, *Geophys. Res. Lett.*, *29*(13), 1624, doi:10.1029/2001GL014397.

Brooks, B. A., J. H. Foster, M. Bevis, L. N. Frazer, C. J. Wolfe, and M. Behn (2006), Periodic slow earthquakes on the flank of Kilauea Volcano, Hawai'i, *Earth Planet. Sci. Lett.*, *246*(3–4), 207–216, doi:10.1016/j.epsl.2006.03.035.

Brooks, B. A., J. Foster, D. Sandwell, C. J. Wolfe, P. Okubo, M. Poland, and D. Myer (2008), Magmatically triggered slow slip at Kilauea Volcano, Hawaii, *Science*, *321*(5893), 1177, doi:10.1126/science.1159007.

Cayol, V., J. Dieterich, A. Okamura, and A. Miklius (2000), High magma storage rates before the 1983 eruption of Kilauea, Hawaii, *Science*, *288*(5475), 2343–2346, doi:10.1126/science.288.5475.2343.

Cervelli, P., P. Segall, F. Amelung, H. Garbeil, C. Meertens, S. Owen, A. Miklius, and M. Lisowski (2002a), The 12 September 1999 upper East Rift Zone dike intrusion at Kilauea Volcano, Hawaii, *J. Geophys. Res.*, *107*(B7), 2150, doi:10.1029/2001JB000602.

Cervelli, P., P. Segall, K. Johnson, M. Lisowski, and A. Miklius (2002b), Sudden aseismic fault slip on the south flank of Kilauea Volcano, *Nature*, *415*(6875), 1014–1018, doi:10.1038/4151014a.

Cervelli, P., A. Miklius, D. Swanson, and A. Douglas (2003), Rethinking the standard model of Kilauea's south flank deformation, *Eos Trans. AGU*, *84*(46), Fall Meet. Suppl., Abstract V11G–04.

Desmarais, E., and P. Segall (2007), Transient deformation following the 30 January 1997 dike intrusion at Kilauea Volcano, Hawaii, *Bull. Volcanol.*, *69*(4), 353–363, doi:10.1007/s00445-006-0080-7.

Dieterich, J. (1988), Growth and persistence of Hawaiian volcanic rift zones, *J. Geophys. Res.*, *93*(B5), 4258–4270, doi:10.1029/JB093iB05p04258.

Dieterich, J. (1994), A constitutive law for rate of earthquake production and its application to earthquake clustering, *J. Geophys. Res.*, *99*(B2), 2601–2618, doi:10.1029/93JB02581.

Dvorak, J., A. Okamura, T. English, R. Koyanagi, J. Nakita, M. Sako, W. Tanigawa, and K. Yamashita (1986), Mechanical response of the south flank of Kilauea Volcano, Hawaii, to intrusive events along the rift systems, *Tectonophysics*, *124*(3–4), 193–209, doi:10.1016/0040-1951(86)90200-3.

Farr, T., and M. Kobrick (2000), Shuttle radar topography mission produces a wealth of data, *Eos Trans. AGU*, *88*(48), 583.

Fukuda, J., and K. Johnson (2008), A fully Bayesian inversion for spatial distribution of fault slip with objective smoothing, *Bull. Seismol. Soc. Am.*, *98*(3), 1128–1146, doi:10.1785/0120070194.

Hansen, P. (1992), Analysis of discrete ill-posed problems by means of the l-curve, *SIAM Rev.*, *34*(4), 561–580, doi:10.1137/1034115.

Langbein, J. (2010), Computer algorithm for analyzing and processing borehole strainmeter data, *Comput. Geosci.*, *36*(5), 611–619, doi:10.1016/j.cageo.2009.08.011.

Larson, K., A. Miklius, and M. Poland (2010), Volcano monitoring using GPS: The June 2007 intrusion and eruption at Kilauea Volcano, Hawai'i, *J. Geophys. Res.*, *115*, B07406, doi:10.1029/2009JB007022.

Lichten, S., and J. Border (1987), Strategies for high-precision Global Positioning System orbit determination, *J. Geophys. Res.*, *92*(B12), 12,751–12,762, doi:10.1029/JB092iB12p12751.

Lisowski, M., D. Dzurisin, R. Denlinger, and E. Iwatsubo (2008), Analysis of GPS-measured deformation associated with the 2004–2006 dome-building eruption of Mount St. Helens, Washington, *U.S. Geol. Surv. Prof. Pap.*, *1750*, 301–316.

Miklius, A., P. Cervelli, M. Sako, M. Lisowski, S. Owen, P. Segal, J. Foster, K. Kamibayashi, and B. Brooks (2005), Global Positioning System measurements on the island of Hawai'i: 1997 through 2004, *U.S. Geol. Surv. Open File Rep.*, *2005-1425*, 1–48.

Miyazaki, S., J. McGuire, and P. Segall (2003), A transient subduction zone slip episode in southwest Japan observed by the nationwide GPS array, *J. Geophys. Res.*, *108*(B2), 2087, doi:10.1029/2001JB000456.

Mogi, K. (1958), Relations between the eruptions of various volcanoes and the deformations of the ground surfaces around them, *Bull. Earthquake Res. Inst. Univ. Tokyo*, *36*, 111–123.

Montgomery-Brown, E., P. Segall, A. Miklius, P. Cervelli, and D. Shelly (2009), Kilauea slow slip events: Identification, source inversions, and relation to seismicity, *J. Geophys. Res.*, *114*, B00A03, doi:10.1029/2008JB006074.

Montgomery-Brown, E., D. Sinnett, M. Poland, P. Segall, T. Orr, H. Zebker, and A. Miklius (2010), Geodetic evidence for en echelon dike emplacement and concurrent slow-slip during the June 2007 intrusion and eruption at Kilauea Volcano, Hawai'i, *J. Geophys. Res.*, *115*, B07405, doi:10.1029/2009JB006658.

Murray, J., and P. Segall (2005), Spatiotemporal evolution of a transient slip event on the San Andreas fault near Parkfield, California, *J. Geophys. Res.*, *110*, B09407, doi:10.1029/2005JB003651.

Nelder, J., and R. Mead (1965), A simplex method for function minimization, *Comput. J.*, *7*(4), 308–313. doi:10.1093/comjnl/7.4.308.

Niell, A. (1996), Global mapping functions for the atmosphere delay at radio wavelengths, *J. Geophys. Res.*, *101*(B2), 3227–3246, doi:10.1029/95JB03048.

Okada, Y. (1985), Surface deformation due to shear and tensile faults in a half-space, *Bull. Seismol. Soc. Am.*, *75*, 1135–1154.

Owen, S., P. Segall, M. Lisowski, A. Miklius, M. Murray, M. Bevis, and J. Foster (2000a), January 30, 1997 eruptive event on Kilauea Volcano, Hawaii, as monitored by continuous GPS, *Geophys. Res. Lett.*, *27*(17), 2757–2760, doi:10.1029/1999GL008454.

Owen, S., P. Segall, M. Lisowski, A. Miklius, R. Denlinger, and M. Sako (2000b), Rapid deformation of Kilauea Volcano: Global positioning system measurements between 1990 and 1996, *J. Geophys. Res.*, *105*(B8), 18,983–18,998, doi:10.1029/2000JB900109.

Phillips, K., C. Chadwell, and J. Hildebrand (2008), Vertical deformation measurements on the submerged south flank of Kīlauea volcano, Hawai'i reveal seafloor motion associated with volcanic collapse, *J. Geophys. Res.*, *113*, B05106, doi:10.1029/2007JB005124.

Poland, M., A. Miklius, T. Orr, A. J. Sutton, C. Thornber, and D. Wilson (2008), New episodes of volcanism at Kilauea Volcano, Hawaii, *Eos Trans. AGU*, *89*(5), 37, doi:10.1029/2008EO050001.

Ryan, M. P. (1987), Neutral buoyancy and the mechanical evolution of magmatic systems, in *Magmatic Processes: Physicochemical Principles*, edited by B. O. Mysen, *Spec. Publ. Geochem. Soc.*, 1, 259–288.

Ryan, M. P. (1988), The mechanics and three-dimensional internal structure of active magmatic systems: Kilauea Volcano, Hawaii, *J. Geophys. Res.*, *93*(B5), 4213–4248, doi:10.1029/JB093iB05p04213.

Segall, P., and M. Matthews (1997), Time dependent inversion of geodetic data, *J. Geophys. Res.*, *102*(B10), 22,391–22,409, doi:10.1029/97JB01795.

Segall, P., E. Desmarais, D. Shelly, A. Miklius, and P. Cervelli (2006), Earthquakes triggered by silent slip events on Kilauea Volcano, Hawaii, *Nature*, *442*, 71–74, doi:10.1038/nature04938.

Swanson, D. A., W. A. Duffield, and R. S. Fiske (1976), Displacement of the south flank of Kilauea Volcano, Hawaii: The result of forceful intrusion of magma into the rift zones, *U.S. Geol. Surv. Prof. Pap.*, *963*, 1–39.

Welstead, S. T. (1999), *Fractal and Wavelet Image Compression Techniques*, 232 pp., SPIE Opt. Eng. Press, Bellingham, Wash., doi:10.1117/3.353798.

Wolfe, C., B. Brooks, J. Foster, and P. Okubo (2007), Microearthquake streaks and seismicity triggered by slow earthquakes on the mobile south flank of Kilauea Volcano, Hawai'i, *Geophys. Res. Lett.*, *34*, L23306, doi:10.1029/2007GL031625.

K. M. Larson, Department of Aerospace Engineering Sciences, UCB 429, University of Colorado at Boulder, Boulder, CO 80309-0429, USA.

A. Miklius and M. P. Poland, U.S. Geological Survey, Hawaiian Volcano Observatory, Hawai'i National Park, HI 86718, USA.

E. K. Montgomery-Brown, Department of Geoscience, 1215 W. Dayton St., Madison, WI 53706, USA. (emilymb1@gmail.com)

P. Segall and D. K. Sinnett, Department of Geophysics, Stanford University, 397 Panama Mall, Stanford, CA 94305, USA.